Fracture phenomena of disordered media

Chung, Jim

4

SCALING OF THE FAILURE STRESS OF HOMOPHASE AND HETEROPHASE 3D SPRING NETWORKS

4.1 INTRODUCTION

The basic question addressed in this chapter is: what is the difference in strength between a large and a small disordered structure loaded under uniaxial compression? If the material would be perfectly homogeneous, no particular difference in local stress and strain fields will be observed. An infinite linear elastic material would even be infinitely strong and such a system can support arbitrarily large loads. To predict, within a physical description, a limit in strength a certain non-linearity has to be considered, like cracks that extend under increasing mechanical load. Even for perfectly linear elastic systems these defects make the material essentially non-linear. For finite systems size effects on the failure stress come about as a direct consequence of the existence of defects like cracks on a micro-scale. If a difference in strength is encountered as a function of size, it is due to the fact that the proportion between the length scale at which fracture originates and propagates with respect to the macroscopic size of the structure alters if the size is enlarged. Therefore, the ability of accommodating local failure, i.e. a redistribution of

mechanical energy in the local surroundings, does not depend only on the intrinsic material properties, but also on extrinsic factors, such as boundary conditions, size and geometry of the specimen.

This work concentrates on the fracture behavior of highly porous disordered media so as to mimic ceramic extrudates that are commonly used as catalyst carriers. The porosity of these extrudates is about 70 volume%. In particular, catalyst carriers should also be strong enough to withstand the applied load under operating conditions of a (petro-)chemical plant[1]. The main objective in this field of research is to access by a modeling approach how microstructural features affect the final failure distribution. Elastic networks of springs are frequently used to model the relation between the mechanical properties and the microstructure of (highly) porous media. In this work disordered three-dimensional spring networks [2, 3] are used to study the size effect in brittle failure. In the past simulations were carried out both in two [4, 5, 6, 7] and three[8, 9, 10, 11, 12, 13] dimensions, mainly exploring regular spring networks. In general, the research so far on size effects [14,15] and fracture growth [16], seems to underline the importance of heterogeneities in random resistor network models[17]. Further, experimental and numerical investigations of size-effects have been pursued in the field of concrete fracture mechanics using deterministic models[18,19].

In order to incorporate a specific microstructure of highly porous ceramic media, we explore a method of generating dynamically a node distribution. This rather mesoscopic approach provides a possibility to incorporate microstructural properties. It is important to realize that any strength distribution during the fracturing process is due to the node distribution itself. So, even a homophase sample may not be homogeneous in strength neither on a local or global scale.

4.2 COMPUTATIONAL PROCEDURE

4.2.1 GENERATION OF NETWORK

The computational procedure starts with the generation of a node distribution. The molecular dynamics based algorithm uses N void volume spheres, which all have a Lennard-Jones interacting outer surface. The method provides a

convenient way of generating a distribution of disordered nodes. The disorder is controlled by the pre-set values of the temperature and pressure thermostat [20]. The radii of the void volume spheres are taken 25 nm and the Lennard-Jones [21]outer surface interaction, σ_{LJ}, is also set to 25 nm. The temperature of the reference bath is 8.0 ε/k_B, (0.78 ε/k_B is the Lennard-Jones triple point temperature with ε the energy and k_B Boltzmann's constant) and the pressure reference bath is pre-set to the value of 0.4 $\varepsilon/\sigma^3_{LJ}$ (1.275 is the Lennard-Jones triple point pressure). Those values are found to be sufficient to generate a disordered spatial distribution [22] of particles.

The relaxation process took 25000 time steps in order to attain equilibrium using a time increment step Δt of 10^{-9} s. The leap-frog integration sheme[18] calculates the position and velocities of the particles using the Newtonian equations of motion. The driving force for each particle in each step is the superposition of all the interactions of the particle with its neighboring particles. After the first 20000 time steps, 8 node distributions are sampled. All the distributions are taken with 2000 consecutive time steps in between. For each combination of width: depth: height in total nine distribution are generated to attain a better representation of the equilibrated disordered system.

The thermostat maintains a constant pressure in the mesoscopic particle system, achieving this by adjusting the box size. To remove the effect of the node density all the node distributions are scaled to an average node density of 500 nodes/μm^3 resulting in an average spacing in 3D of 0.125 μm.

The generated distributions form the basis of the spring connecting procedure. Every node is a potential point of connection and as a consequence the geometry of the network is globally fixed by the positions of the nodes. Actually, only the interaction length between the nodes is left as a parameter. The node interaction between two nodes exists only if their relative distance is below the connectivity threshold, C_0. Depending on the value of C_0, the system may develop from fully connected, i.e. every node is connected with all the other nodes, to the lower limit where all nodes are disconnected. For low C_0 the network resembles the Delaunay network, whereas for higher C_0 values the

network geometry will deviate more and more from it. In this investigation C_0 is 0.15 μm. This value is one of the lowest C_0 value that could be addressed, while remaining a network with a constant average node density.

4.2.2 COMPRESSION OF NETWORK

In the following the spring networks are loaded in compression and after each force increment, the network configuration with the lowest energy is calculated. The total elastic energy is described by a two-body central force (CF), a three-body bond bending (BB) and a four-body torsion (T) contribution[3]

$$U_{EL} = U_{CF} + U_{BB} + U_T \tag{4.1}$$

The central reaction force contribution on node i, $\Delta F_i^{CF}(n+1)$ with respect to the previous force, $\Delta F_i^{CF}(n)$, is given by the first derivative of the central force potential U_{CF} with respect to the node position of *i*, q_i, i.e.:

$$\Delta F_i^{CF,q}(n+1) = -[-\frac{\partial U^{CF}(n+1)}{\partial q_i}] = -k_{ij}^{CF}\left[\Delta\vec{u}_{ij}(n+1).\hat{R}_{ij}(n)\right]\hat{R}_{ij}^{q}(n) \tag{4.2}$$

where the CF potential is described by:

$$U^{CF}(n+1) = \frac{1}{2}\sum_{<ij>} k_{ij}^{CF}\left[\Delta\vec{u}_{ij}(n+1).\hat{R}_{ij}(n) + (\left|\vec{R}_{ij}(n)\right| - \left|\vec{R}_{ij}(0)\right|\right]^2 \tag{4.3}$$

The <*ij*> denotes the summation over all *ij* pairs of connected nodes. The bond vector $\vec{R}_{ij}(n)$ from node *i* to node *j* (≡ bond *ij*) at increment *n* is defined as $\vec{R}_{ij}(n) = \vec{r}_j(n) - \vec{r}_i(n)$, ($\hat{R}_{ij} = \vec{R}_{ij} / \left|\vec{R}_{ij}\right|$) where $\vec{r}_j(n)$ is the position of node *j* at increment *n*. Furthermore, the displacement increment $\Delta\vec{u}_{ij}(n)$ at increment *n* is given by $\Delta\vec{u}_j(n) - \Delta\vec{u}_i(n)$, where $\Delta\vec{u}_i(n) \equiv \vec{u}_i(n+1) - \vec{u}_i(n)$ is the bond displacement increment of node *i* and $\vec{u}_i(n) \equiv \vec{r}_i(n) - \vec{r}_j(0)$ represents the displacement of node *i* at increment *n*. The force constant for the CF ~follows from the uniaxial straining of a bar of length $\left|\vec{R}_{ij}(0)\right|$ with Young's modulus *E* and cross-sectional area A_{ij} :

$$k_{ij}^{CF} = \frac{A_{ij}E}{|\vec{R}_{ij}(0)|} \tag{4.4}$$

The magnitude of the force constant is inversely proportional to the initial bond length.

For the bond bending potential (the three-body term), between nodes *ijk*, where *i* is the center of the hinge like bond bending potential, U_{BB}, the following expression is used:

$$U_{BB}(n+1) = \frac{1}{2} \sum_{<ijk>} k_{ijk}^{BB} [\Delta\theta_{ijk}^{ij}(n+1) + \Delta\theta_{ijk}^{ik}(n+1) + \theta_{ijk}(n)]^2 \qquad (4.5)$$

$\Delta\theta_{ijk}^{ij}(n+1)$ and $\Delta\theta_{ijk}^{ik}(n+1)$ are the angular deviations in step *n+1*, due to beam like bending of the bond *ij* and *ik*. The force constant

$$k_{ijk}^{BB} = (\frac{1}{k_{ijk}^{ij}} + \frac{1}{k_{ijk}^{ik}})^{-1} \qquad (4.6)$$

with k_{ijk}^{ij} and k_{ijk}^{ik} are taken from elasticity theory of a bending beam. The first component is given by :

$$k_{ijk}^{ij} = \frac{3EI_{ij}}{|\vec{R}_{ij}(n)|} \qquad (4.7)$$

with I_{ij} is the second moment of area of bond *ij*. The second one k_{ijk}^{ik} of bond *jk* is found similarly.

The torsion interaction, U_T, along the bond *ik* due to the relative motions of bond *ij* and bond *kl* is a pseudo four body potential. When bonds *ij* and *kl* are projected on a plane perpendicular to the bond vector *ik*, this yields a three-body problem, $j-i-k-l \rightarrow (j-i'-l)$ with $i' = (ik)$. The torsion potential is therefore actually an (*ik*)*jl* bond bending potential in the *ik*-plane, where (*ik*) stands for the point in the *ik*-plane where bond *ik* intersects the *ik*-plane. The potential can now be written as

$$U_T(n+1) = \frac{1}{2} \sum_{<ijkl>} k_{ijkl}^{T} [\Delta\Phi_{ijkl}(n+1) + \Phi_{ijkl}(n)]^2 \qquad (4.8)$$

and Φ_{ijkl} is the angle in the *ik*-plane projected system. Like for bond bending, the torsion force constant is taken from elasticity theory and is defined as

$$k_{ijkl}^{T} = \frac{EI_{ik}}{(1+\nu)\,|\,\vec{R}_{ik}(n)\,|} \tag{4.9}$$

where ν is Poisson's ratio.

When all the node-node interactions are added into the global matrix, a system of $3N$ (N being the number of spheres) linear equations is formed, or $\Delta\vec{F}(n+1) = [K]\Delta\vec{u}(n+1)$, where $\Delta\vec{F}(n+1)$ is a $3N$-dimensional vector of the applied force increments at compression step n, $[K]$ the $3N$x$3N$ stiffness matrix and $\Delta\vec{u}(n+1)$ $3N$-dimensional vector of the displacement increments in the compression step n. The external force is applied through the force vector. The resulting displacement increments are obtained by solving the system of equations using a preconditioned conjugate gradient algorithm, which exploits the fact that $[K]$ is a sparse matrix. The new positions at the end of increment $n+1$ are updated according to $\vec{r}_i(n+1) = \vec{r}_i(n) + \Delta\vec{u}_i(n+1)$.

The fracture criterion used throughout this chapter is the maximum strain of 0.25%. The same value is also applied as fracture criterion for bond length and angular distortion. Once the fracture strain is satisfied in a spring element, the bond is removed from the network. Nodes without connection (floating nodes) or groups of unconnected nodes (fragments) are also removed from the interaction matrix. As a result of the removal of floating nodes and fragments, the possible effects of these fragments on the actual failure stress are explicitly ignored. An exception is maintained for the first layer on top and the last layer at the bottom of the sample with a thickness of 10 nm. All connections emerging from the nodes lying within these two layers are not subjected to fracture. This is done to take into account the fragmentation effect at the contact area. Actually, these un-removed nodes will effectively transmit the load similar to the ability of the fragments to transmit the load in real experiments.

4.3 RESULTS

Various specimens with different base areas are constructed, namely 0.64, 1.44, 2.56, 5.76 μm^2. In addition, the size effect is explored by generating samples of different heights, thus leading to different aspect ratios.

Table 4.1

Overview of the total number of configurations examined for a particular combination of base area and height

height (μm) / base (μm^2)	0.8	1.2	1.6	2.4	3.2	4.8	6.4
0.64	9	9	8	8	9		
1.44	8	9	8	8	8	10	5
2.56	8	8	7	7	6	8	4
5.76	6	3	8	3	5	3	

The various configurations are listed in Table 4.1. An example of an intermediate stage in the fracturing process is displayed in Figure 4.1 (base area 2.56 μm^2 and height 2.4 μm). The radius of the cross-section of the bonds in the network is 0.1 μm and the Young's modulus is set to be 400 GPa. Throughout the calculations the node density is kept constant, that is 500 nodes per μm^3. Using these properties the calculations lead to a failure stress of the order of 10 MPa, which is reasonable for highly porous ceramic materials[23].

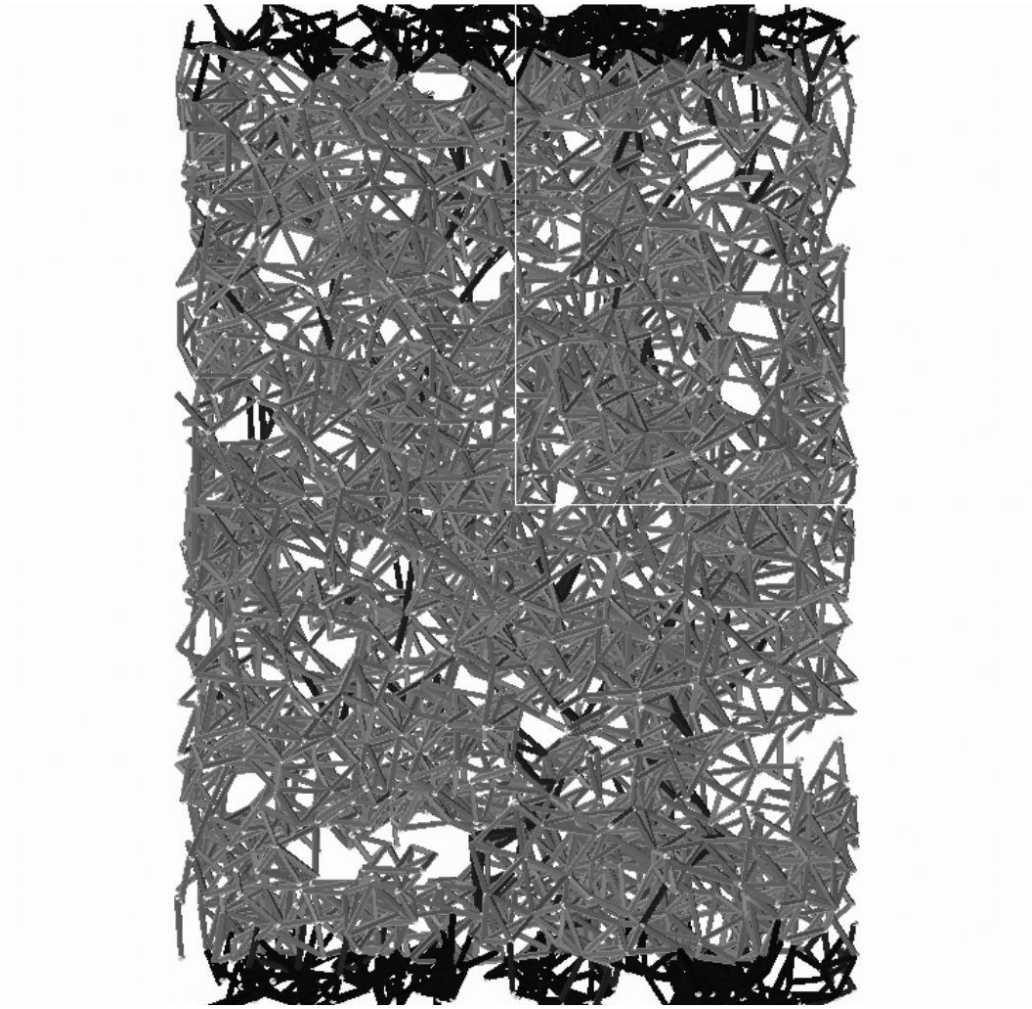

Figure 4.1. Intermediate stage in the fracturing process of a sample with a base area of 2.56 μm^2 and a height of 2.4 μm. Red bonds fulfill the fracture criterion. For colored representation see Chapter 7.

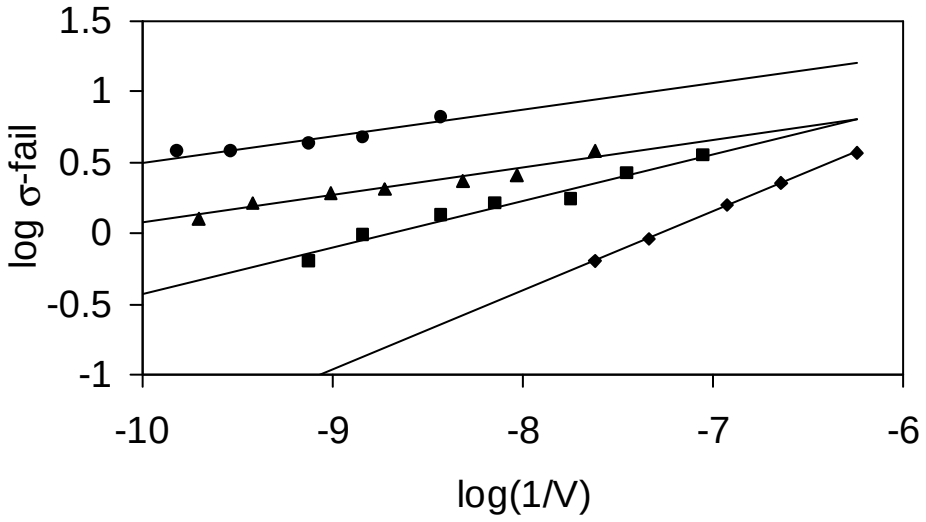

Figure 4.2. Double-log plot of failure stress (MPa) vs. reciprocal volume (in units of 10^{-3} μm^3) for various base areas (◆: 0.64 μm^2; ■: 1.44 μm^2; ▲: 2.56 μm^2; ●: 5.76 μm^2).

The overall volume effect on the failure stress, σ_{fail}, shows a Weibull[24] behavior as depicted in Figure 4.2. In the weakest-link assumption by Weibull, fracture initiation leads to immediate global failure. The probability, $g(\sigma)$, that fracture will initiate locally at a stress σ is described by a power law behavior, $g(\sigma) = \sigma^m$, where m is the so-called Waybill modulus reflecting the materials properties. The cumulative failure distribution is expressed by:

$$F_V(\sigma) = 1 - e^{-cL^d \sigma^m} \qquad (4.10)$$

For a volume L^d and where c is a geometrical constant and d represents the dimensionality. The cumulative failure probability goes to unity for $\sigma \to \infty$. However, if the sample size increases $F(\sigma)$ shifts towards lower values of σ and the failure probability becomes of the order of unity for even smaller values of the stress. The expectation value of the failure distribution $\sigma_{fail\text{-}W}$ (taken here as

the median value) predicts a dependence of the failure stress on the size according to: $\sigma_{fail\text{-}W} \sim L^{-d/m}$ for a d-dimensional space of linear size L.

Figure 4.3 displays the volume dependence of failure stress according to the description based on extreme statistics as developed by Duxbury–Leath[16] and Ray-Chakrabarti[25,26]. Although it also based on a weakest-link assumption, but here the chance that fracture will initiate locally at a stress σ is described by

$$g(\sigma) = e^{-\frac{k}{\sigma_\mu}} \tag{4.11}$$

leading to a failure distribution of the form:

$$F_V = 1 - \exp\left[-cL^d \exp\left(-\frac{k}{\sigma^\mu}\right)\right] \tag{4.12}$$

and an expectation value

$$\sigma_{fail-D-L} = k^{1/\mu}\left(\log L^d + \log c - \log\log 2\right)^{-1/\mu} \tag{4.13}$$

It is interesting to note that the failure of hierarchical structures of fiber bundles under equal load sharing [27] leads to $\sigma_{\text{fail}} \sim \left(\log\log L^d\right)^{-1}$. Like in the Weibull case, for extremely large size L, $F(\sigma) \cong 1$ for non-vanishing stress. It may be noted that although in the Weibull distribution the failure probability is unity as $\sigma \to \infty$ for any size, this is not necessarily the case for Eq. (4.10)unless the system size becomes very large.

The Duxbury-Leath and Ray-Chakrabarti analyses are related to the Gumbel[28] form used in fracture reliability analysis. However, the latter is based on a weakest link argument that assumes that all parts of the material carry the same stress. Eq. (4.11) and Eq. (4.12) assume that failure is initiated by load hotspots. Actually, in contrast, to earlier studies [4,23], the results displayed in 4.2 and Figure 4.3 do not validate either the Gumbel distributions or the Weibull distributions.

Table 4. 2

Coordination number and the parameters μ for homophase materials .

base area (μm^2)	0.64	1.44	2.56	5.76
coordination number CN_{Dis}	3.03	3.16	3.22	3.8
standard deviation CN_{Dis}	0.07	0.07	0.08	0.07
μ	0.66	1.01	1.69	1.82

The effect of the volume on the failure stress is strongly affected by the local coordination number CN_{Dis} of the disordered phase. The latter increases with increasing base area (see Table 4.2). As expected also the failure stress increases with increasing coordination number. In addition to a homophase material represented by a distribution of disordered nodes also composite materials are studied.

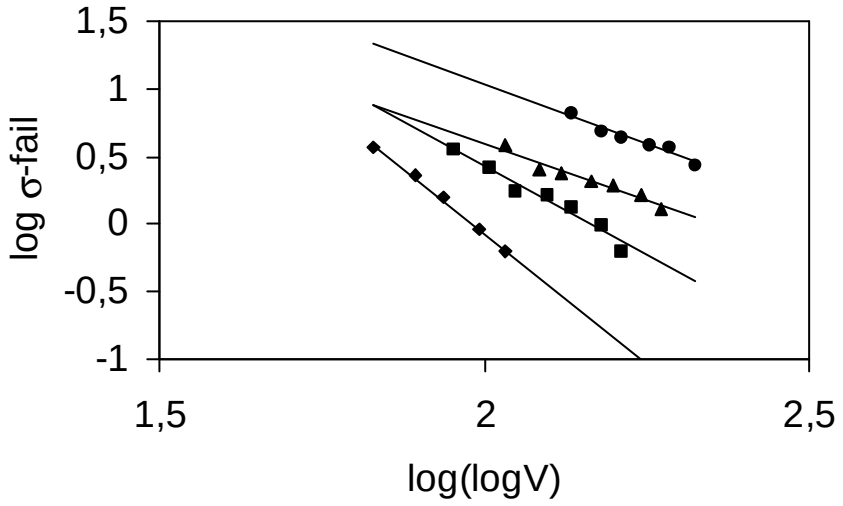

Figure 4.3. Double-log plot of failure stress (MPa) vs. the logarithm of the sample volume (in units of 10^{-3} μm^3) for various base areas (◆: 0.64 μm^2; ■: 1.44 μm^2; ▲: 2.56 μm^2; ●: 5.76 μm^2).

They are composed of a slab with thickness d_S of an ordered material that separates two regions of a disordered phase. The base area is kept constant, being 0.64 μm². Figure 4.4 displays the density as a function of the height and it indicates the position of the slice of the ordered material.

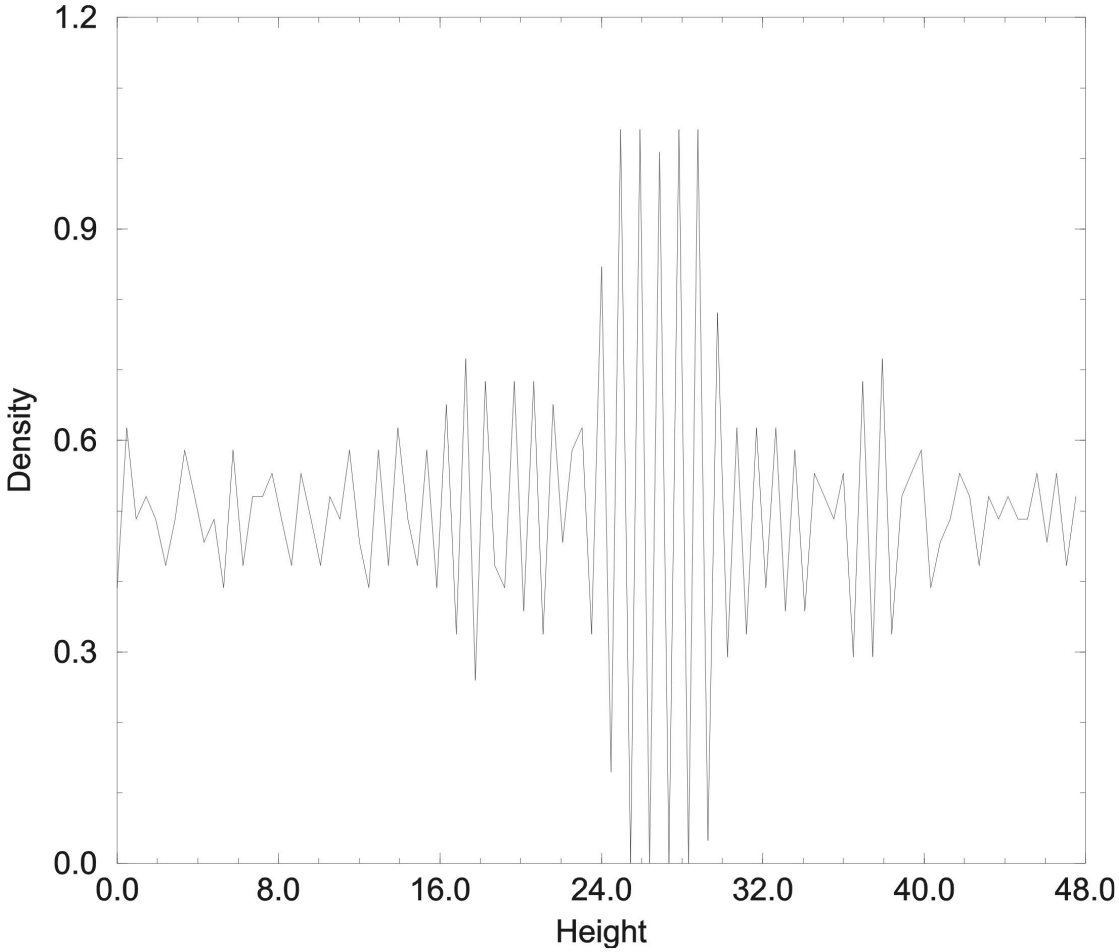

Figure 4.4. The density as a function of the sample height (in units of 0.1 μm) in the case of a composite material.

In Table 4.3, the coordination number of the slab, CN_S, is estimated by assuming the following relationship: $hCN=d_SCN_S+(h-d_S)CN_{Dis}$. The failure stress of the composite materials differs considerably from that of the homophase materials (see Table 4.3). In fact, the composite materials show an increase in strength by a factor of 4, in comparison to the disordered structures

of the same size, i.e. even if the composite phase is compared with the homophase specimens of the effective height, $h_{eff} = h - h_{slab}$.

Table 4.3

Heterophase and homophase samples

(base area is 0.64 μm² and CN_{Dis} in the homophase system)

	homophase	heterophase	homophase	heterophase
Height (μm)	3.2	3.2	4.8	4.8
Height slab (μm)		0.72		1.9
CN_S		9.0		5.9
σ_{fail} (MPa)	0.82	3.77	0.66	3.72

Table 4 4

Heterophase and homophase samples with an effective height h_{eff} (h-h_{slab})

h (μm)	3.2	4.8
h_{eff} (μm)	2.5	2.9
σ_{fail} (MPa) of the disordered phase with h_{eff}	0.94	0.87

4.4 DISCUSSION AND CONCLUSIONS

Generally speaking, the size effect on the failure stress of disordered networks studied here can be described equally well by both the Weibull and Gumbel

failure distributions. Although the failure stress depends on the volume, the precise geometry of the specimen proves to be an important factor as well. The size effect is stronger for lower coordination number and it seems to diminish for larger values of the coordination number. A quantitative influence of the height on the failure stress can be estimated as follows. The probability P of a defect of a certain size n in a volume L^d can roughly be estimated by $P(n) \cong L^d p^n$ (with a site probability p)[29]. Because the probability of a largest defect is of the order 1, the largest defect scales as $n_{largest} = -d(LogL/\log p)$ and the failure stress is proportional to $n_{largest}^{-1/\mu}$. The exponent μ may vary between 1 and 4, depending on the dimensionality and the interactions involved. In principle these considerations were already made in [30]. Arguments that lead to this scaling behavior are based on the scaling behaviour of a typical defect size that is responsible for global failure. In our case it leads to height dependence at constant base area, according to:

$$\sigma_{fail} \propto \left(log \frac{h}{\xi} \right)^{-1/\mu} \tag{4.14}$$

where ξ represents the correlation length within the sample. Here, the correlation length is a constant within the same base as can be concluded from the small standard deviation in the coordination number (Table 4.2). In Figure 4.5a and Figure 4.5b the height dependence of σ_{fail} is displayed and it can be concluded that σ_{fail} scales logarithmically with the height, according to Eq. (4.1). It was reported previously[31] that the macroscopic voltage at which a random fuse network fails can be described by a similar logarithmic dependence (Eq. (4.1)) and μ was found to be approximately 1.25.

However, here μ appears to depend sensitively on the system size. In our case μ ranges between 0.7 for the smallest system (base area 0.64 μm^2) and 1.8 for the largest system (base area 5.76 μm^2) (see Table 4.2). This sounds reasonable when evaluating the upper and lower bounds of μ, which depend on the dimensionality d of the problem and the possible interactions between the local cracks. Within the framework of classical fracture mechanics, with a stress field near the tip of a crack of length l that scales with the applied stress according to $\sigma\sqrt{l}$, the stress fields at a crack tip becomes proportional to $\sigma n^{1/4}$ (with n the

'size' of the defect) and μ is equal to 4 (for a penny-shaped defect of size 2*l* and $n = \pi l^2$).

In general, for systems with non-interacting defects in a network described by central forces, $\mu = 2(d-1)$. Indeed simulation studies of the fracture strength distribution of a 2D triangular network of randomly diluted bond percolating systems showed that the Gumbel distribution with μ=2 fits the data better than the Weibull distribution. [32,33], even up to the percolation limit. If in a 2D triangular network also bond-bending forces are included the same conclusion can be drawn for increasing disorder and μ becomes unity. However, for the fracture strength distribution of super-elastic 2D networks it was observed that the Weibull distribution gives a better description than the Gumbel distribution.

If the concentration of cracks increases, the interaction between these defects will cause that the stress at the crack tip depends on the size of the defects *n*. Assuming a linear scaling, the stress at the crack tip becomes proportional to σ*n* and that μ becomes closer to unity. For smaller systems when local interactions between the defects are more likely to occur one expects a smaller value for μ around unity depending on the details of the force fields in the network. Indeed, an increase of μ with sample size to 4 (for central forces only) is found in this work (see Table 4.2). It is interesting to note that μ for the smallest volumes studied here is 0.7, i.e. much smaller than what one would expect when only central forces are included. This lower value is likely the result of the fact that the total elastic energy is described by two-body central force, three-body bond bending and four-body torsion contributions. It gives rise to a more substantial overlap of localized stress fields for smaller sizes.

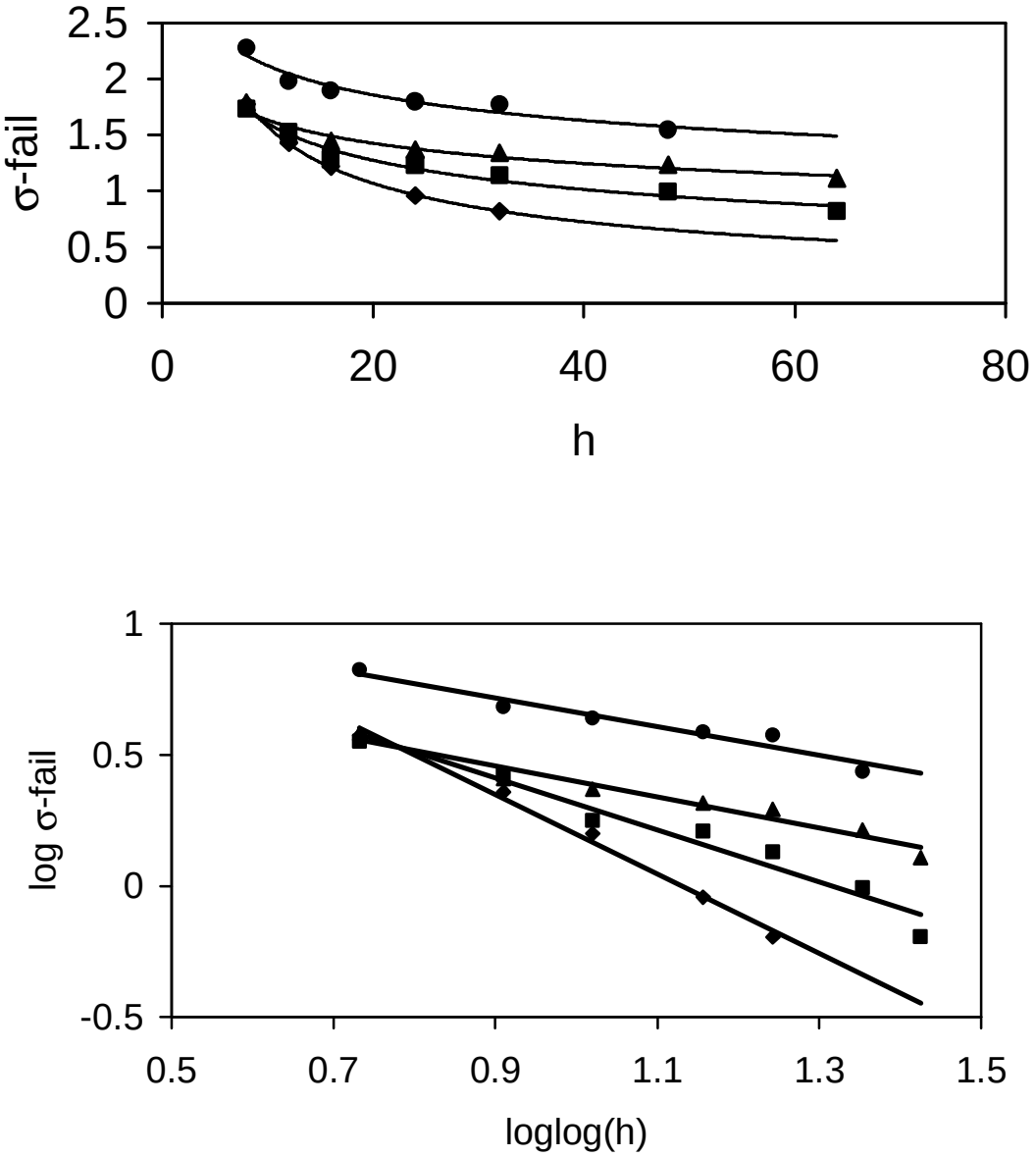

Figure 4.5. (a) plot of failure stress (MPa) versus height (in units of 0.1 μm) for various base areas (◆: 0.64 μm^2; ■: 1.44 μm^2; ▲: 2.56 μm^2; ●: 5.76 μm^2); (b) plot of the logarithm of the failure stress (MPa) versus the double logarithm of the height (in units of 4.5(a)) for various base areas.

Because of the size dependence of μ one should be careful in extrapolating these findings, as cast in Eq. (4.14) to all kinds of microstructures and composite materials. Only for highly porous ceramic materials that show brittle failure, a size dependence of the failure stress described by Eq. (4.14) is experimentally confirmed. Because of plasticity this is not the case for comparable structures like metallic foams in which failure mechanisms even differ in compression (buckling of the struts) compared to tension (fracture of the struts). So, the overall size dependence, including the size dependence of μ, is strongly affected by the type of failure mechanism and the local microstructure as is reflected in Table 4.2 by the coordination number. Further, it may be argued that Eq. (4.14)is actually more complex and that μ could still be considered in fact independent of the sample size and the logarithmic dependence is only the leading term in this equation. So, the values of μ listed in Table 4.2 are actually effective values and within the same kind of failure mechanism and microstructure the exponent μ becomes more or less universal. However, correction terms would be necessary to include that cannot really be neglected for other systems. Such correction-to-scaling terms can be quite significant (see, for example, Refs. [8] and [32]. Actually, Figure 4.5b already hints to such a possibility, as the *log* of the stress failure versus the double *log* of *h* does not really produce a perfect straight line for the case of a base area of 1.44 μm^2.

In conclusion we may state that the modulus μ in the Gumbel failure distribution appears to depend on the system size because of the decrease of interactions between the defects with increasing height. However, in all cases thin (in the loading direction) samples are stronger than thick samples under uni-axial compression and the failure stress increases with increasing coordination number. If height is increased, the onset of ultimate failure takes place earlier because the number of possible critical crack paths is increased. Within the framework of the weakest link principle we may say that with increasing size the weakest link will be weaker. Therefore the strength decreases with increasing height and this will ultimately lead to a vanishing strength at infinite thickness. With increasing base area, i.e. for broader samples, also there the chance that fracture is initiated in a larger sample is bigger than in a smaller sample. But, the load bearing capacity increases with

the sample width and it results in a finite strength for an infinitely broad sample. The latter can also be argued based on classical fibre bundle models [34].

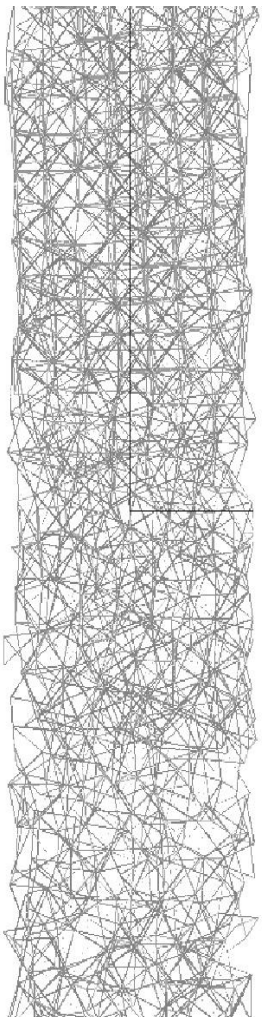

Figure 4.6. A heterophase three-dimensional network: base area is 0.64 μm^2 and height is 4.8 μm.

Further, it can be concluded that the failure stress of a heterophase material, composite material, differs considerably from that of a homophase materials (see Table 4). The composite materials show an increase in strength by a factor of 4 in comparison to the disordered structures of the same size. The actual enhancement in strength due to the slab depends on the thickness of the slab. In

fact, the size of a heterophase sample could have chosen 15 to 25 times larger than a homophase disordered structure while retaining the same strength.

However, the actual failure stress of the composite material depends critically on the details of the configuration. Figure 4.4 shows a layering effect of the disordered region near the ordered phase, together with the formation of clusters in the disordered phase.

In Figure 4.6 the layering and the clustering effects are also visible for the case of a heterophase three-dimensional network with a base area of 0.64 μm^2 and height of 4.8 μm. This layering effect in the radial distribution is similar to the observation of density oscillations at liquid surfaces in bulk recrystallization and surface melting, found both experimentally[35,36] and theoretically [37,38]. The solid induces a layer-like density oscillation in the liquid with a periodicity that depends on the wave vector where the structure factor has it strongest peak. The density profile of Figure 4.4 as a function of the distance r from the interface at r_0 can be described by

$$\rho(r) = \rho_0 + 0.5\left\{ e^{-\frac{r-r_0}{\xi}} \cos\left[\frac{2\pi}{a}\left(r - r_0\right)\right]\right\} \qquad (4.15)$$

where ρ_0 is the density fluctuation of the disordered phase and a is the periodicity of the interlayer spacing in the ordered phase. ξ is the correlation length in the disordered system and ξ^{-1} reflects the degree of disorder at the interface. The form of Eq. (4.2) is typically what one should expect from a mean field treatment [39,40]. Global fracture of the composite material occurs in the disordered phase because it represents the weakest part of the material. However, because of these layering effects around the interfaces with the ordered phase, i.e. including the ordered clusters that appear in the disordered system, the relevant height for fracture is much smaller than the height simply described by $h_{eff} = h - h_{slab}$. On average, the largest height of the fully disordered phase in Figure 4.4 is about 0.5 μm (see also Figure 4.6), corresponding to a failure stress of at least 2.5 MPa as estimated from Figure 4.5. This value must be considered as a lower bound because of the details in the configurations. Nevertheless, it is much closer to the actual result of the

calculation (Table 4.3) than predictions based on $h_e - h_{slab}$ (Table 4.4) and it underlines the importance of the density fluctuations near the various interfaces in these composite materials.

4.5 REFERENCES

[1] I.C. van den Born, A. Santen, H.D. Hoekstra and J.Th.M. De Hosson, Phys. Rev.B, 43, 3794 (1991).

[2] B. K. Chakrabarti, L.Gilles Benguigui, Statistical Physics of fracture and breakdown in disordered systems, Clarendon Press, Oxford, 1997.

[3] J.W. Chung, A. Roos, J.Th.M. De Hosson, and E. van der Giessen, Phys. Rev. B 54,15094 (1996).

[4] I.C. van den Born, A. Santen, H.D. Hoekstra, and J.Th.M. De Hosson, in Fracture Processes in concrete, Rock and Ceramics, edited by J.J.M. van Mier, J.G. Rots, and A. Bakker (E & FN SPON, London, 1991), p. 231.

[5] S. Feng, P.N. Sen, B.I. Halperin, and C.J. Lobb, Phys. Rev. B 30, 5386 (1984).

[6] H.J. Hermann, A. Hansen, and S. Roux, Phys. Rev. B 39, 637 (1989).

[7] S. Arbabi and M.Sahimi, Phys. Rev. B 38, 7173 (1988).

[8] M. Sahimi and S. Arbabi, Phys. Rev. B 47, 695 (1993).

[9] S. Arbabi and M. Sahimi, Phys. Rev. B 41, 772 (1990).

[10] S. Arbabi and M. Sahimi, Phys. Rev. B 38, 7173 (1988).

[11] S. Arbabi and M. Sahimi, Phys. Rev. Lett. 65, 725 (1990).

[12] J. Wang, J. Phys. A 22, L291 (1989).

[13] S. Arbabi and M. Sahimi, J. Phys. A 23, 2211 (1990).

[14] B. Kahng, G.G. Batrouni, S. Redner, L. de Arcangelis and H.J. Herrmann, Phys Rev B 37, 7625 (1988).

[15] P.M. Duxbury, P.D. Beale and C. Moukarzel, Phys. Rev. B 51, 3476 (1995).

[16] P.L. Leath and P.M. Duxbury, Phys. Rev. B 49, 14905 (1994).

[17] H.J. Hermann, S. Roux, Editors, Statistical models for the fracture of disordered media, North Holland, Amsterdam, 1990, and references therein.

[18] M.R.A. van Vliet and J.G.M. van Mier, in Material instabilities in solids , eds. R. de Borst and E. van der Giessen, Wiley, New York, 1998, p. 185.

[19] A. Carpinteri, Editor: Size-scale effects in the failure mechanisms of materials and structures, E&FN SPON, London, 1996, and references therein.

[20] H.J.C. Berendsen, J.P.M. Postma, W.F. van Gunsteren, A. DiNola and J.R. Haak, J.Chem.Phys.81(8), 3684 (1984).

[21] M.P. Allen and D.J. Tildesley, Computer Simulations of Liquids (Oxford University Press, Oxford, 1992).

[22] J.W. Chung, J.Th.M. De Hosson and E. van der Giessen, Phys. Rev. B, 2001, in press.

[23] J.-j. Aue, J.Th.M. De Hosson, J. Mat. Science, 33, 5455-5462 (1998).

[24] W. Weibull, Ingeniörsvetenskapsakadiems, Handlingar, nr 151, pp.1 (1939).

[25] P.Ray and B.K. Chakrabarti, solid State Communications 53,477 (1985).

[26] B.K. Chakrabarti, in: Non-linearity and breakdown in soft condensed matter, ed. K.K. Bardan, B.K. Chakrabarti, A. Hansen, Lecture Notes in Physics, vol 437, Springer, Heidelberg, p. 171.

[27] W.I. Newman and A.M. Gabrielov, Intern. J. of Fracture, 50,1(1991)

[28] E.J. Gumbel, Statistics of extremes, Columbia University press, NY, 1958.

[29] D. Stauffer, Introduction to percolation theory, Taylor and Francis, London, 1985.

[30] P.M. Duxbury, P. L. Leath, P.D. Beale, Phys.Rev, 36,367 (1987).

[31] B. Kahng, G.G. Batrouni, S. Redner, L. de Arcangelis, H.J. Hermann, Phys.Rev.B37,7625 (1988).

[32] M. Sahimi and S. Arbabi, Phys. Rev. 77,713 (1993).

[33] P.D. Beale and D. Srolovitz, Phys.Rev. 37, 5500 (1988).

[34] H.E. Daniels, Proc. Roy. Soc. London, A183,404 (1945).

[35] H. Reichert, O. Klein, H. Dosch, M. Denk, V. Honklmaki, T. Lippmann, G. Reiter, Nature, 408, 839 (2000).

[36] W.J. Huisman, J.F. Peters, M.J. Zwanenburg, S.A. de Vries, T.E. Derry, D. Aberanathy, J.F. van der Veen, Nature, 390,379 (1997).

[37] R.L. Davidchack, B.B. Laird, J. Chem.Phys. 108,9457 (1998).

[38] J.Q. Broughton, G.H. Gilmer, J. Chem. Phys. 84, 5749 (1986).

[39] O. Tomagnini, F. Ercolessi, S. Iarlori, F.D. Di Tolla, E. Tosatti, Phys. Rev. Lett., 76, 1118 (1996).

[40] P. Tarazona, L. Vidente, Mol. Phys. 56, 557 (1985).